






Cross-section Measurement of the Cosmologically Relevant ${}^7\text{Be}(n, \alpha){}^4\text{He}$ Reaction over a Broad Energy Range in a Single Experiment

L. Lamia^{1,2} , M. Mazzocco^{3,4}, R. G. Pizzone², S. Hayakawa⁵, M. La Cognata², C. Spitaleri^{1,2}, C. A. Bertulani⁶ , A. Boiano⁷, C. Boiano⁸, C. Brogini⁴, A. Cacioli^{3,4}, S. Cherubini^{1,2}, G. D'Agata^{1,2,13} , H. da Silva⁹, R. Depalo^{3,4}, F. Galtarossa¹⁰, G. L. Guardo^{1,2}, M. Gulino^{2,11}, I. Indelicato^{1,2}, M. La Commara^{7,12}, G. La Rana^{7,12}, R. Menegazzo⁴, J. Mrazek¹³, A. Pakou¹⁴, C. Parascandolo⁷, D. Piatti^{3,4}, D. Pierroutsakou⁷, S. M. R. Puglia², S. Romano^{1,2}, G. G. Rapisarda², A. M. Sánchez-Benítez¹⁵, M. L. Sergi², O. Sgouros^{2,14}, F. Soramel^{3,4}, V. Soukeras^{2,14}, R. Spartá^{1,2}, E. Strano^{3,4}, D. Torresi², A. Tumino^{2,11}, H. Yamaguchi⁵, and G. L. Zhang¹⁶

¹ Dipartimento di Fisica e Astronomia “E. Majorana”, Univ. degli Studi di Catania, Catania, Italy

² INFN-LNS, Laboratori Nazionali del Sud, Catania, Italy

³ Dipartimento di Fisica e Astronomia, Univ. di Padova, Padova, Italy

⁴ INFN-Sezione di Padova, Padova, Italy

⁵ Center for Nuclear Study, University of Tokyo, Japan

⁶ Department of Physics and Astronomy, Texas A&M University-Commerce, Commerce, TX, USA

⁷ INFN-Sezione di Napoli, Napoli, Italy

⁸ INFN-Sezione di Milano, Milano, Italy

⁹ Laboratório de Instrumentação, Engenharia Biomédica e Física da Radiação (LIBPhys-UNL), Departamento de Física, FCT-UNL, 2829-516 Monte da Caparica, Portugal

¹⁰ INFN-Laboratori Nazionali di Legnaro, Legnaro, Italy

¹¹ Facoltà di Ingegneria e Architettura, Università degli Studi di Enna Kore, Italy

¹² Dipartimento di Farmacia, Università di Napoli “Federico II”, Italy

¹³ Nuclear Physics Institute of the Czech Academy of Science, Rez, Czech Republic

¹⁴ Department of Physics and HINP, University of Ioannina, Greece

¹⁵ Departamento de Ciencias Integradas y Centro de Estudios Avanzados en Física, Matemáticas y Computación, Facultad de Ciencias Experimentales, Universidad de Huelva, E-21071 Huelva, Spain

¹⁶ School of Physics, Beihang University, Beijing 100191, People’s Republic of China

Received 2019 March 6; revised 2019 May 10; accepted 2019 May 10; published 2019 June 28

Abstract

Studying interactions of radioactive ions with neutrons is particularly demanding and has been performed only in a few cases. Some of these interactions are crucial in several astrophysical contexts. In the present work, the case of the ${}^7\text{Be}$ destruction induced by the (n, α) reaction is investigated at the energies typical of the primordial nucleosynthesis by means of the Trojan Horse Method applied to the ${}^2\text{H}({}^7\text{Be}, \alpha\alpha)\text{p}$ quasi-free reaction. The ${}^7\text{Be}(n, \alpha){}^4\text{He}$ cross-section has been measured in a single experiment from ~ 2 MeV down to cosmological energies. The corresponding deduced reaction rate has been adopted to evaluate the impact on big bang nucleosynthesis and on the lithium problem.

Key words: nuclear reactions, nucleosynthesis, abundances – primordial nucleosynthesis

1. Introduction

Among the three pillars on which the big bang theory is based, the big bang nucleosynthesis (BBN) is the one probing the universe at the earliest time, about 2–3 minutes after the cosmological bang. Together with the existence of the cosmic microwave background (CMB) radiation, which tells us about a 300,000 yr old universe, and the Hubble expansion rate, it is possible to finally draw an exhaustive picture of the beginning of our universe. For this reason, BBN is matter of efforts and studies, since it can help us to understand the early epoch of our universe. The elegant formalism of the standard BBN model (often referred to as SBBN) allows one to derive the primeval abundances of the elements (mostly helium-4, deuterium, helium-3, and lithium) by invoking the single free baryon-to-photon ratio $\eta = n_b/n_\gamma$ parameter, once the neutron lifetime (τ_n), the number of neutrino families (N_ν), and the nuclear reaction network have been fixed (see for instance Bertulani & Kajino 2016; Pitrou et al. 2018). Since SBBN predicts light element abundances by varying η , it is necessary to devise a way to fix its value. For this purpose, the most followed way is the use of deuterium abundance as the “best baryometer” (Steigman 2006), since after its synthesis during SBBN, there is

no known production site or mechanism. Conversely, deuterium can only be destroyed during stellar evolution, thus its primordial abundance is determined from high-redshift (cosmological) clouds on the line of sight of quasars (Steigman 2006; Pettini & Cooke 2012; Pitrou et al. 2018). Starting from these considerations, it is then possible to fix the η value and further infer the remaining primordial abundances (i.e., helium-3, helium-4, and lithium). Additionally, existing ${}^3,4\text{He}$ primordial observations are in agreement with BBN predictions (see, for instance, Cooke 2015 and Izotov et al. 2014). However, the global picture remains incomplete because of the lithium abundances, as the metal-poor halo stars observations disagree by a factor of ~ 3 with respect to the those inferred from the SBBN model.

Possible solutions have been proposed, such as a different number of neutrino families or a revision of neutron lifetime. Thanks to the precise LEP measurements for neutrino families, leading to the value of $N_\nu = 2.9840 \pm 0.0082$ (LEP Collaborations 2006), and to the neutron lifetime measurements, leading to the value of $\tau_n = 880.2 \pm 1.0$ s (Patrignani & Particle Data Group 2016), only η enters in the BBN primordial abundance calculations for which the corresponding uncertainties are only related to the uncertainties affecting the cross

section measurements (Pitrou et al. 2018). In addition, the precision era enabled by studies on the CMB anisotropies by the *Wilkinson Microwave Anisotropy Probe* and *PLANCK* missions (Weiland et al. 2011; Ade et al. 2016) allowed for independent η determinations, leading to the currently accepted value of $\eta = \eta_{\text{CMB}} = (6.07 \pm 0.07) \times 10^{-10}$ (Ade et al. 2016). Combining η_{CMB} with the evaluated BBN abundances, it has been then possible to infer the primeval abundances for light nuclei and compare these values with the corresponding astronomical observations in properly selected astrophysical environments. To date, although such a comparison shows a strong agreement for deuterium and helium-isotopes, lithium continues to be a matter of discussion (Pitrou et al. 2018). Lithium abundances are derived from metal-poor halo-star observations; an averaged value of $(\text{Li}/\text{H})_{\text{obs.}} = (1.58^{+0.35}_{-0.28}) \times 10^{-10}$ is currently accepted, as reported in Sbordone et al. (2010). By comparing $(\text{Li}/\text{H})_{\text{obs.}}$ with the most recent inferred lithium abundances $(\text{Li}/\text{H})_{\text{BBN}} \sim (5.623) \times 10^{-10}$ (Pitrou et al. 2018), a factor of ~ 3.6 shows up.

Besides the recently proposed stellar physics solutions of Fu et al. (2015), Nordlander et al. (2012) attributed the origin of the discrepancy to the interplay between depletion mechanisms and/or enrichment due to interstellar gas, or theoretical description involving variation of the nucleon velocity distribution at BBN energies (as suggested in Hou et al. 2017) or the needs of physics solutions outside the Standard Model (see for instance Coc et al. 2013; Cyburt et al. 2013; Goudelis et al. 2016). Overall, the search of nuclear physics solutions has triggered several works in the last years.

Among these, nuclear physics processes involving the unstable ${}^7\text{Be}$ ($t_{1/2} = 53.22 \pm 0.06$ days) are of particular interest. In more detail, at η_{CMB} ${}^7\text{Li}$ is mainly produced from ${}^7\text{Be}$ that undergoes the electron capture process $e^- + {}^7\text{Be} \rightarrow {}^7\text{Li} + \nu_e$ at late times (i.e., long after the ${}^7\text{Be}$ synthesis). One thus expects that the primordial ${}^7\text{Li}$ abundance is essentially determined by the beryllium-7 production and destruction rates at the temperatures $T = 20\text{--}70$ keV at which ${}^7\text{Be}$ is synthesized in the early universe (Broggini et al. 2012). The dominant BBN ${}^7\text{Be}$ producing channel, i.e., the ${}^3\text{He}(\alpha, \gamma){}^7\text{Be}$ reaction, has been studied in Bemmerer et al. (2006) and di Leva et al. (2009), leading to an overall uncertainty of about 7% (Broggini et al. 2012), thus making it a poor possible solution to the lithium problem. Furthermore, the destructive ${}^7\text{Be}(d, p)2\alpha$ channel has also been investigated without any significant impact on the lithium problem solution (see Pitrou et al. 2018 for details). Most recently, the measurement of Rijal et al. (2018) evaluated the impact of a new resonance at ~ 360 keV; although it increases the total ${}^7\text{Be}(d, p)2\alpha$ reaction rate, its contribution is not sufficient for solving the lithium problem. Additional solutions have been proposed, such as the recent study of Hartos et al. (2018) to investigate the role of the ${}^{11}\text{C}$ levels intervening in the ${}^7\text{Be}(\alpha, \gamma){}^{11}\text{C}$; they concluded that these channels play a minor role in the lithium problem. Similar conclusions were drawn in Hammache et al. (2013) about the search of possible ${}^{10,11}\text{C}$ resonant states of interest for lithium nucleosynthesis.

In the last 5 years many works have been published regarding the ${}^7\text{Be}$ destruction channels involving neutrons, i.e., the ${}^7\text{Be}(n, p){}^7\text{Li}$, and ${}^7\text{Be}(n, \alpha){}^4\text{He}$ reactions. In particular, the (n, α) reaction channel has been the subject of recent studies (Hou et al. 2015; Barbagallo et al. 2016; Kawabata et al. 2017; Lamia et al. 2017).

Hou et al. (2015) is based on the application of the charge-symmetry hypothesis (CSH) to the ${}^4\text{He}(\alpha, p){}^7\text{Li}$ data of King et al. (1977) and Slobodrian et al. (1975), and to the ${}^7\text{Li}(p, \alpha){}^4\text{He}$ data of Cassagnou et al. (1962), giving the absolute ${}^7\text{Be}(n, \alpha){}^4\text{He}$ cross-section values for the p -wave component only. The cross-section measurement of Barbagallo et al. (2016) was performed at the n_TOF facility, allowing for the measurement of the s -component of the ${}^7\text{Be}(n, \alpha){}^4\text{He}$ cross section at energies lower than 10 keV by means of a neutron beam impinging on a radioactive ${}^7\text{Be}$ target. Starting from their partial cross-section measurement, they calculated the total direct radiative capture (DRC) reaction cross section at energies lower than 10 keV (see Barbagallo et al. 2016 for details). The most recent ${}^7\text{Be}(n, \alpha){}^4\text{He}$ cross section measurement of Kawabata et al. (2017) relied on the reverse reaction ${}^4\text{He}(\alpha, n){}^7\text{Be}$ allowing for an investigation of the ${}^7\text{Be}$ - n interaction at energies of $E_{\text{c.m.}} = 0.20\text{--}0.81$ MeV, getting information both on the ${}^7\text{Be}$ ground and first excited state contributing to the (n, α) channel.

In Lamia et al. (2017) we deduced the ${}^7\text{Be}(n, \alpha){}^4\text{He}$ reaction cross section at BBN energies by applying the CSH to the available ${}^7\text{Li}(p, \alpha){}^4\text{He}$ experimental data studied via the Trojan Horse Method (THM). This study allowed us to cover, with a single experiment, a wide energy range from ~ 3 MeV down to BBN energies. Our measurements agree, within the uncertainties, with the direct measurements of Hou et al. (2015) and Kawabata et al. (2017). In the present paper we are going to present a new cross-section measurement of the ${}^7\text{Be}(n, \alpha){}^4\text{He}$ performed via the THM applied to the quasi-free ${}^2\text{H}+{}^7\text{Be}$ reaction. In the following, the details about the method, the experiment, and the data analysis will be given together with the implications for BBN.

2. Basic Features of the THM

The THM is an indirect technique allowing measurement of the cross section of a two-body reaction $A(x, c)C$ by properly selecting the quasi-free component of a suitable $2 \rightarrow 3$ body reaction $a(A, c)Cs$ (Baur 1986; Spitaleri 1991; Spitaleri et al. 2004; Tribble et al. 2014; Spitaleri et al. 2016). By referring to the pole diagram of Figure 1, nucleus a is chosen because of its large $a = x \oplus s$ configuration, its relatively low $x - s$ binding energy, and its known radial wavefunction for the $x - s$ configuration. It represents the so-called ‘‘Trojan-horse nucleus.’’ The $2 \rightarrow 3$ reaction is induced at energies well above the Coulomb barrier of the $A + a$ interacting particles in order to induce the sub-process $A - x$ in the nuclear field. Thus, the breakup of a is quasi-free because only cluster x takes part in the binary process, while the other counterpart s acts as spectator, i.e., it maintains in the exit channel the same momentum distribution it had inside a before its break up. In addition, a specific role is played by the $x - s$ binding energy, as pointed out in Spitaleri et al. (2016) and Tribble et al. (2014). In particular, it compensates for the projectile energy down to low, i.e., astrophysically relevant, energies, thus making it of immediate help for nuclear astrophysics purposes. In particular, since the $A - x$ interaction occurs directly in the nuclear field, no Coulomb barrier penetration effects or screening phenomena (Assenbaum et al. 1987) affect the THM data, in comparison with the direct impacts where these two effects cause the well-known exponential decrease of the cross-section values and the enhancement of the cross-section values, respectively.

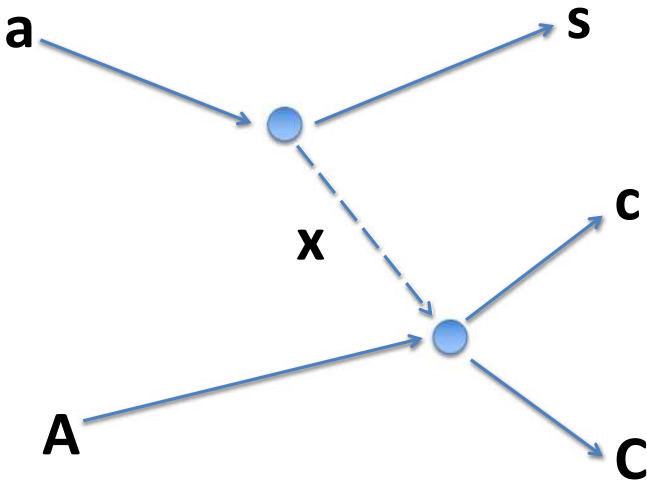


Figure 1. Pole diagram for the quasi-free $a(A, c)S$ reaction, s being the so-called *spectator*, while x represents the *participant* to the astrophysically relevant $A(x, c)C$ reaction.

In the most simple theoretical description of THM by means of the plane wave impulse approximation, the cross section of the quasi-free $a(A, c)S$ reaction can be related to the one of the binary $A(x, c)C$ processes via the formula (Tribble et al. 2014; Spitaleri et al. 2016)

$$\frac{d^3\sigma}{dE_c d\Omega_c d\Omega_C} \propto \text{KF} \cdot |\Phi(\mathbf{p}_{xs})|^2 \cdot \left. \frac{d\sigma}{d\Omega} \right|_{\text{cm}}^{\text{HOES}}, \quad (1)$$

where

1. KF represents the kinematical factor, depending on the masses, momenta, and angles of the outgoing particles, that takes into account the final-state phase space factor;
2. $|\Phi(\mathbf{p}_{xs})|^2$ is the square of the Fourier transform of the radial wavefunction describing the $x-s$ intercluster motion, usually in terms of Hankel, Eckart, or Hulthen functions, depending on the $x-s$ system.
3. $d\sigma/d\Omega|_{\text{cm}}^{\text{HOES}}$ is the half-off-energy-shell (HOES) differential cross section for the two-body reaction at the center-of-mass energy $E_{\text{cm}} = E_{cC} - Q$, where Q represents the Q -value of the HOES $A(x, c)C$ reaction while E_{cC} represents the relative $c-C$ energy measured in laboratory. The deduced cross section is HOES because in the entrance channel, the transferred particle x having mass m_x is *virtual*, thus its energy and momentum are not related by the mass-shell equation $E_x = k_x^2/(2m_x)$. Under QF conditions, the relative $A-x$ energy is then determined by relation $E_{Ax} = p_{Ax}^2/(2\mu_{Ax}) - \epsilon_{xx}$, with ϵ_{xx} being the binding energy of the TH-nucleus. In the exit channel, the relation is restored because the emitted $c-C$ particles are real (see Tribble et al. 2014 for details).

The abovementioned technique allowed the study of astrophysically relevant reactions, as discussed in Lamia et al. (2015), La Cognata et al. (2013), and Sergi et al. (2015). More advanced techniques have also been developed as reported, for instance, in Mukhamedzhanov et al. (2008) and La Cognata et al. (2011), in which a modified R-matrix approach was followed for studying multiresonant reactions of interest for astrophysics, and in the case of the recent works of Tumino et al. (2018), Guardo et al. (2017), and Indelicato et al. (2017). Recently, an extension to RIB’s charged-particle-induced

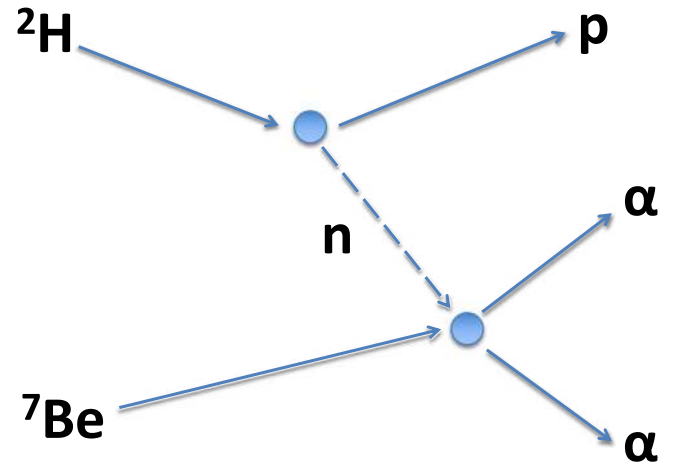


Figure 2. Pole diagram for the quasi-free ${}^2\text{H}({}^7\text{Be}, \alpha\alpha)\text{p}$ reaction. Nucleus ${}^2\text{H}$ represents the adopted TH-nucleus that undergoes quasi-free break-up interacting with the ${}^7\text{Be}$ beam. The neutron acts as the *participant* of the ${}^7\text{Be}$ (n, α) ${}^4\text{He}$ binary process, while the proton is the *spectator*.

reactions was also provided, as discussed in Cherubini et al. (2015) and Pizzone et al. (2016).

3. The Experiment

The ${}^2\text{H}({}^7\text{Be}, \alpha\alpha)\text{p}$ experiment was performed at the EXOTIC facility (Farion et al. 2008) of Laboratori Nazionali di Legnaro (INFN-LNL) using a 20.4 MeV ${}^7\text{Be}$ beam impinging on a CD_2 target with a thickness of $400 \mu\text{g cm}^{-2}$. The quasi-free (QF) ${}^2\text{H}({}^7\text{Be}, \alpha\alpha)\text{p}$ process is represented by the pole diagram of Figure 2 where deuteron undergoes its breakup in neutrons (participant) and protons (spectator). The detection setup was developed with the aim of detecting the two emerging alpha particles while the kinematical quantities of the undetected proton were reconstructed via momentum-energy conservation laws. In addition, since only quasi-free (QF) events were considered for the THM analysis, the setup covered the kinematical region corresponding to the *QF-angular pairs*, i.e., the angular pairs at which the spectator maintains the same momentum distribution it had inside the deuteron before its break up (Tribble et al. 2014; Spitaleri et al. 2016).

The EXOTIC facility is devoted to the in-flight production of light weakly bound RIBs and it has allowed for the production of the unstable ${}^7\text{Be}$ beam in the past (see, for instance, Mazzocco et al. 2013). For this purpose, ${}^7\text{Li}$ ions (150–200 pnA) were delivered by the LNL-XTU Tandem accelerator onto a H_2 gas target to induce the ${}^7\text{Li}(p, n){}^7\text{Be}$ reaction ($Q = -1.64$ MeV). The gas target consisted of a 5 cm long gas cell doubly walled with $2.2 \mu\text{m}$ thick Havar foils and it was filled with 1 bar H_2 gas at cryogenic temperature (90 K), corresponding to a target thickness of about 1.35 mg cm^{-2} . The ${}^7\text{Be}$ secondary beam was separated from the ${}^7\text{Li}$ scattered beam, and from other contaminants, by means of a 30° -bending magnet, a Wien filter, and slit settings and collimation systems located at suitable positions along the beam line (Mazzocco et al. 2013). At the end of the beam line, an intensity of $(5-8) \cdot 10^5$ pps, a purity of about 99%, a beam spot of about 9 mm (FWHM), and an energy spread of about 1 MeV (FWHM) were measured.

A schematic drawing of the adopted experimental setup is given in the upper part of Figure 3, while the lower part shows the experimental apparatus inside the scattering chamber at

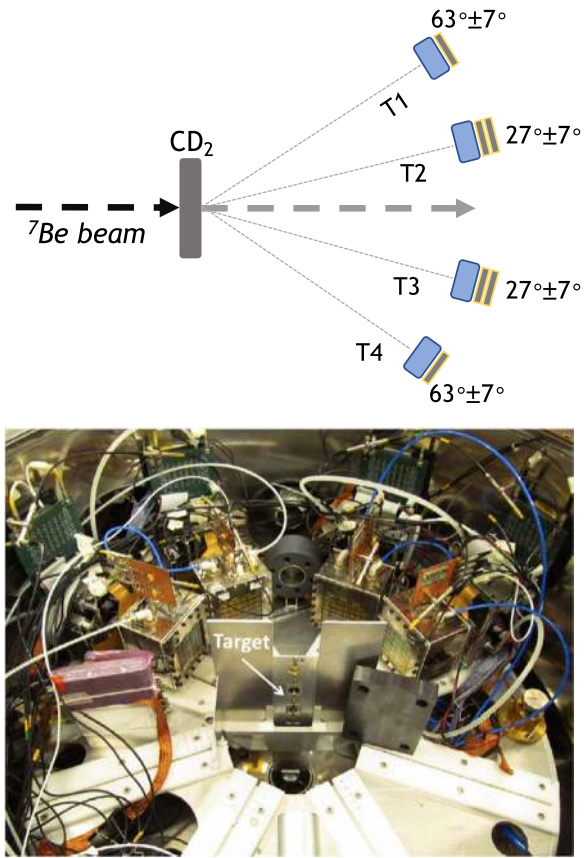


Figure 3. (Upper part) Schematic drawing of the experimental apparatus adopted for the ${}^2\text{H}({}^7\text{Be}, \alpha\alpha)\text{p}$ experiment. The light blue rectangles mark the position of the ionization chambers (IC), while the yellow ones mark those of the DSSSDs. (Lower part) Displacement of the detection system inside the scattering chamber at the final focal plane of the facility EXOTIC at INFN-LNL.

INFN-LNL. It consisted of four modules of the detector array EXPADES (Pierroutsakou et al. 2016) arranged around the QF-angular pairs, according to previous kinematic calculations. In order to double the statistics, a symmetrical configuration was chosen.

The detection of the alpha particles in the angular range $\theta_{\text{lab}} = 20^\circ\text{--}34^\circ$ was accomplished by ΔE - E telescopes placed at a distance of about 16 cm from the target. The telescopes were made up of a Frisch grid ionization chamber (IC), acting as the ΔE stage, a $300\ \mu\text{m}$ Double Sided Silicon Strip Detector (DSSSD) and a further $300\ \mu\text{m}$ PAD Silicon detector to measure the residual energy. Such a solution was chosen for the most forward telescopes T2 and T3 in Figure 3 because α -particles with energy up to ~ 36 MeV were expected. The remaining T1 and T4 telescopes were placed at $\theta_{\text{lab}} = 56^\circ\text{--}70^\circ$ and were assembled as an IC followed by the $300\ \mu\text{m}$ silicon strip detector because low-energy α -particles were expected (i.e., with energies lower than 20 MeV). The DSSSD detectors, placed at distances of about 24 cm from the target, have an active area of $64 \times 64\ \text{mm}^2$, with 16 strips per side orthogonally oriented to define $4 \times 4\ \text{mm}^2$ pixels, thus introducing an angular resolution of about 0.9° (FWHM). Only the coincidences T1–T3 and T2–T4 cover the quasi-free angular region.

The ICs were filled with isobutane gas continuously maintained at the pressure of 100 mbar by a devoted read-out system, while $1.5\ \mu\text{m}$ thick mylar foils were used as entrance

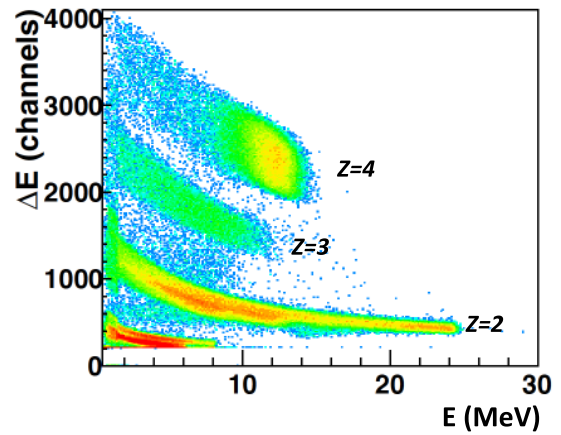


Figure 4. Experimental ΔE - E plot for telescope T2. The $Z = 2$ locus has been selected in coincidence with the events on T4. The $Z = 4$ locus represents the scattered beam on the CD_2 target.

and exit windows. The threshold of ~ 3 MeV introduced by the ICs barely affected the alpha-particle detection at most backward angles, and it did not introduce any threshold for the emitted alpha particles in the forward direction because kinematical calculations predicted energies higher than 5 MeV. A standard three-peak ${}^{239}\text{Pu}$ - ${}^{241}\text{Am}$ - ${}^{244}\text{Cm}$ α source was used for the energy calibration of the DSSSD as well as devoted run measurements using a 10 MeV and a 24 MeV ${}^7\text{Li}$ beam impinging on carbon and CH_2 targets to induce the alpha-producing reactions ${}^{12}\text{C}({}^7\text{Li}, \alpha){}^{15}\text{N}$, $\text{H}({}^7\text{Li}, \alpha){}^4\text{He}$. Additionally, the same α source was adopted for evaluating the energy loss in the ICs to validate the isobutane gas pressure reading as well as the mylar windows thickness.

4. Data Analysis

4.1. Reaction Channel Selection

As a first step of the data analysis, the events belonging to the three-body reaction channel ${}^2\text{H}({}^7\text{Be}, \alpha^4\text{He})\text{p}$ were selected. Using the standard ΔE - E technique to select the $Z = 2$ loci in the IC+DSSSD telescopes (see Figure 4), the alpha-alpha events of interest were reconstructed after the energy loss in the CD_2 target and in the IC was properly evaluated. Additionally, for the most forward detectors, the energy loss of the most energetic (i.e., $E_\alpha > 26$ MeV) alpha particles in the DSSSD was properly taken into account for the complete energy loss correction.

Once the energies and the angles of the detected alpha particles were determined, a complete three-body kinematics was reconstructed by adopting the energy-momentum conservation laws. This allowed us to completely reconstruct the kinematical properties of the *undetected* third particle with the only assumption on its mass (i.e., $m = 1$ in a.m.u.).

For the selected events, the experimental Q -value was then reconstructed, showing an isolated peak reported in Figure 5. A Gaussian fit of the experimental data led to the value of 16.73 ± 0.86 MeV, in agreement with the expected one of 16.766 MeV. The FWHM of the Q -value spectrum (FWHM ~ 2 MeV) reflects the ${}^7\text{Be}$ beam spot (FWHM ≈ 1 MeV) together with energy loss effects in the CD_2 target (≈ 0.7 MeV). Only the events falling inside this peak were considered in the further data analysis. To additionally constrain the reaction channel selection, the experimental

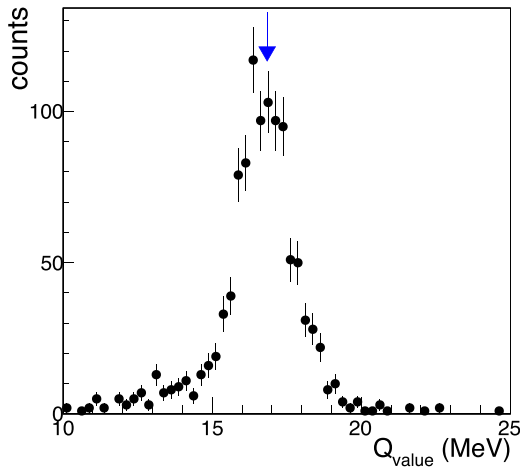


Figure 5. Experimental Q -value spectrum for the ${}^2\text{H}({}^7\text{Be}, \alpha\alpha)\text{p}$ events selected here, centered at 16.76 MeV with a FWHM of ~ 2 MeV. The vertical arrow marks the position of the expected value of 16.766 MeV.

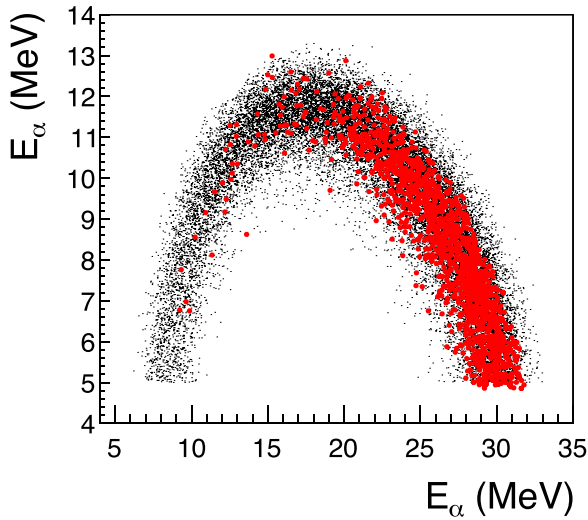


Figure 6. Experimental kinematical locus for the ${}^2\text{H}({}^7\text{Be}, \alpha\alpha)\text{p}$ events (red points) compared with the simulated one in which beam parameters (energy distribution and spot dimension) as well as detection properties (geometry and detection threshold) have been taken into account. The comparison refers to a selected quasi-free angular pair of $\theta_\alpha = 27^\circ \pm 1^\circ$ (horizontal axis) and $\theta_\alpha = 63^\circ \pm 1^\circ$ (vertical axis).

energy values of the detected α particles were compared with that obtained by devoted kinematical calculations for the angular window $\theta_\alpha = 27^\circ \pm 1^\circ$ (as detected in T3) and $\theta_\alpha = 63^\circ \pm 1^\circ$ (as detected in T1). The comparison, shown in Figure 6, strongly confirms the reaction channel selection, as well as the absence of contaminations from other reaction channels.

4.2. Reaction Mechanism Selection

As discussed in Spitaleri et al. (2016) and Tribble et al. (2014), the additional step of a THM analysis is proper reaction mechanism selection. In more detail, the pole diagram shown in Figure 2 represents only the particular reaction mechanism in which we are interested in, i.e., the quasi-free (QF) one, although other reaction mechanisms, leading to the same outgoing particles, could be present. According to the QF-hypothesis, in

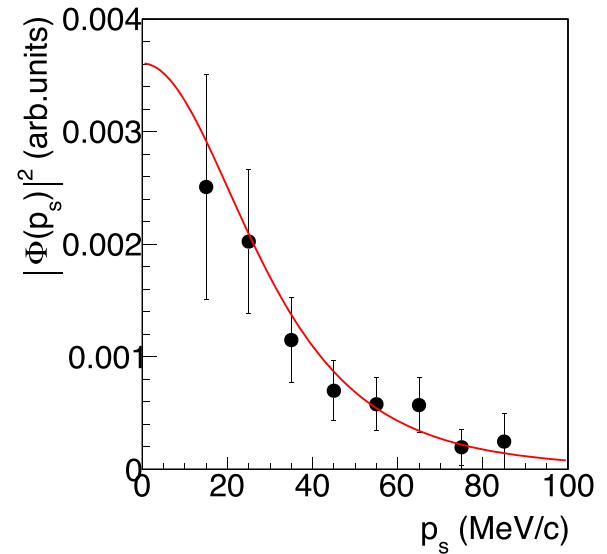


Figure 7. Experimental momentum distribution for the emerging proton in the ${}^2\text{H}({}^7\text{Be}, \alpha\alpha)\text{p}$ reaction (black points), with the corresponding statistical error bar. The experimental data are compared with the squared modulus of the theoretical Hulthén wavefunction in momentum space.

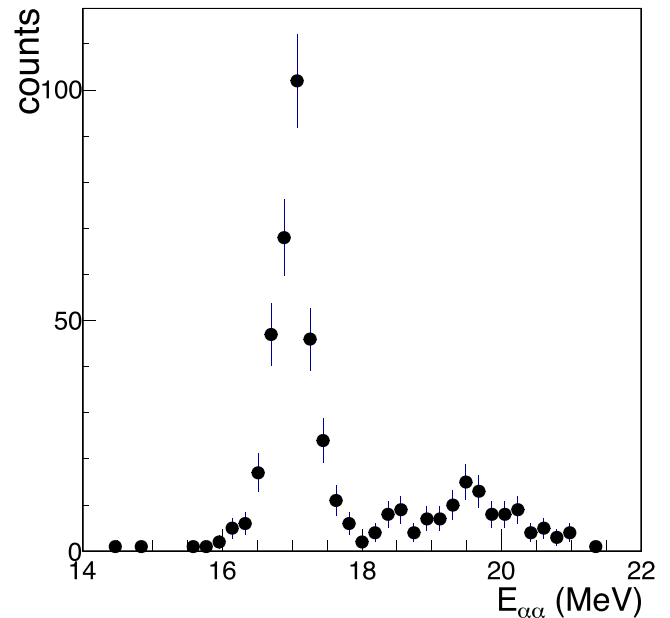


Figure 8. Coincidence yield in the relative energy range of interest for the THM analysis, once the quasi-free component has been disentangled.

the exit channel the *spectator* particle maintains the same momentum distribution it had inside the TH-nucleus before the occurrence of its break-up. A central role in the discussion is played by the FWHM of the momentum distribution, for which a possible variation (i.e., narrowing) could suggest the occurrence of final-state interaction among the detected ejectiles, thus causing a deviation from the pure QF process described by the polar diagram of Figure 2, as discussed in detail in Pizzone et al. (2009).

Thus, owing to its sensitivity to the reaction mechanism, its experimental determination has been extensively reported in different papers and here we limit our discussion to the experimental results. In Figure 7, the obtained experimental

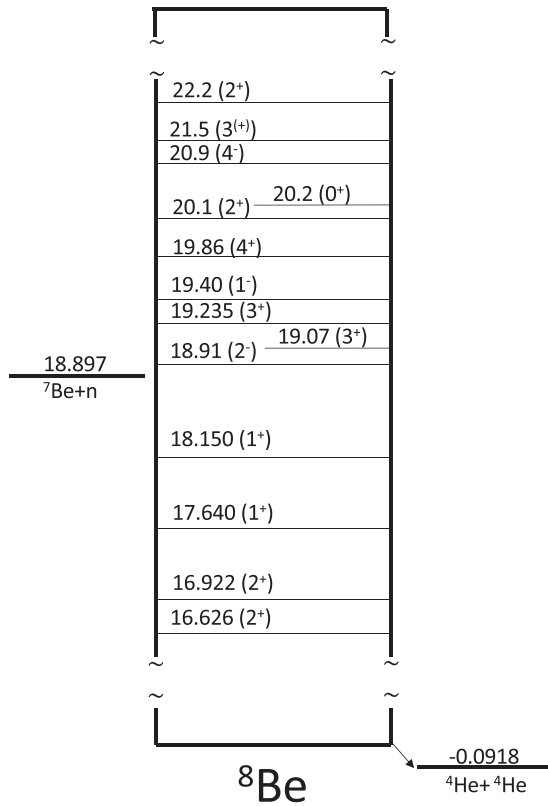


Figure 9. ^8Be energy level diagram extracted from Kelley et al. (2012) and showing the levels of interest for the present investigation.

data (black points with the corresponding statistical uncertainty) are compared with the squared Hulthén wavefunction in momentum space (red curve) describing the s -wave component of the p - n relative motion inside the deuteron, the d -wave being negligible (Lamia et al. 2012). The experimental data refer to the relative energy window of $E_{\alpha\alpha} = 20 \pm 1$ MeV at which the three-body cross section is a slowly varying function of the energy and a significant statistic can be singled out for comparison with the theoretical momentum distribution. The agreement between our data and the theoretical distribution is strong evidence of the presence of the QF-reaction mechanism, thus allowing us to further proceed in the extraction of the $^7\text{Be}(n, \alpha)^4\text{He}$ cross section. These results are also in agreement with the conclusion of Pizzone et al. (2005, 2009), for which the high transferred momentum $q_t \approx 430 \text{ MeV } c^{-1}$ reached in the present experiment justifies a match between the experimental FWHM extracted here and its theoretical asymptotic value of $58 \text{ MeV } c^{-1}$, as reported in Zadro et al. (1989). Additionally, the agreement in Figure 6 suggests that no other mechanism, such as the sequential mechanism, contributes to the reaction yield. However, in order to select the QF mechanism, only events within the momentum range $|p_s| < 50 \text{ MeV } c^{-1}$ have been included in the following steps of the data analysis.

4.3. The Two-body Reaction Cross Section

The selected QF data are shown in Figure 8 as black filled circles, with the corresponding statistical uncertainty, as a function of the kinematic quantity $E_{\alpha\alpha}$ representing the relative energy for the detected alpha particles. The prominent peak at

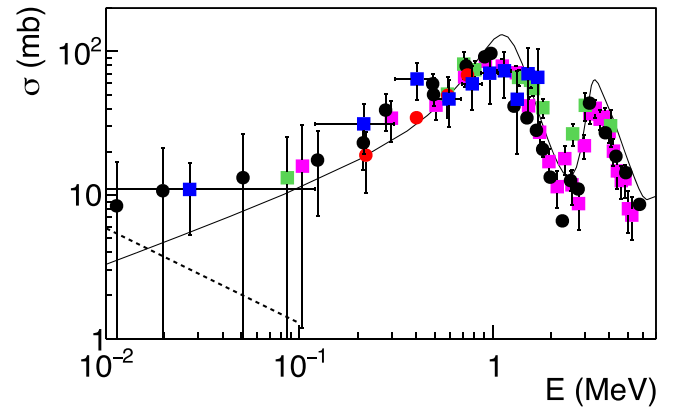


Figure 10. THM $^7\text{Be}(n, \alpha)^4\text{He}$ cross-section measurement (blue points with the statistical error) compared with the direct measurements of Kawabata et al. (2017; red points) and Hou et al. (2015; black points). The magenta and green symbols refer to the reverse measurement obtained in Lamia et al. (2017). The solid line is the ENDF/B-VII.1 evaluation Chadwick et al. (2011) (<https://www.nndc.bnl.gov/sigma>), while the dotted line gives the trend of the direct radiative capture (DRC) cross section given in Barbagallo et al. (2016).

Table 1

Upper, Lower, and Adopted THM Reaction Rates Extracted Here for the $^7\text{Be}(n, \alpha)^4\text{He}$ Reaction, Expressed in $\text{cm}^3 \text{mol}^{-1} \text{s}^{-1}$

T_9	Lower	Adopted	Upper
0.2	0.88×10^6	1.58×10^6	2.27×10^6
0.3	1.26×10^6	2.24×10^6	3.21×10^6
0.4	1.65×10^6	2.87×10^6	4.09×10^6
0.5	2.05×10^6	3.51×10^6	4.96×10^6
1	4.30×10^6	6.90×10^6	9.51×10^7
1.5	6.94×10^6	1.08×10^7	1.46×10^7
2	9.81×10^6	1.51×10^7	2.04×10^7
2.5	1.28×10^7	1.98×10^7	2.70×10^7
3	1.59×10^7	2.51×10^7	3.42×10^7

~ 17 MeV corresponds to the contribution of the 16.626 MeV and 16.922 MeV ($J^\pi = 2^+$) ^8Be excited states, while at higher energies the population of broad levels of ^8Be is evident, as shown also in the ^8Be energy levels diagram of Figure 9 extracted from Kelley et al. (2012). Taking into account the post-form collision prescription (see, e.g., Spitaleri et al. 2016), the present THM experiment allows investigation of the cosmologically relevant $^7\text{Be}(n, \alpha)^4\text{He}$ reaction in a broad center-of-mass energy range, this last quantity being defined as $E_{\text{c.m.}} = E_{\alpha\alpha} - 18.99$ MeV. The HOES $^7\text{Be}(n, \alpha)^4\text{He}$ two-body cross section has been derived by inverting Equation (1) for the previous data above the threshold of 18.99 MeV. At such energies, the influence of broad ^8Be excited levels at about 20 MeV is present. Thus, since our THM experiment relies on the coincidence detection of two α particles, parity conservation requires the occurrence of a p -wave interaction in the entry channel of the $^7\text{Be}(n, \alpha)^4\text{He}$ binary process. Thus, $l = 1$ angular distributions were assumed for the THM data integration. Indeed, due to low statistics, we could only extract the cross section integrated over the range 100° – 150° . Consequently, any possible contribution of additional partial waves intervening in the $^7\text{Be}(n, \alpha)^4\text{He}$ process could not be ruled out in the present experiment. Then, our data differ from those integrated over the whole solid angle by a constant factor.

Table 2
Lithium Abundances Calculated via the BBN Code of Kawano (1988) with the Nuclear Inputs of Pizzone et al. (2014) (Labeled as Pizz2014)

Reaction Rate	${}^7\text{Li}/\text{H}$	${}^7\text{Be}/\text{H}$	$({}^7\text{Li}/\text{H} + {}^7\text{Be}/\text{H})$
Pizz2014+Hou2015	2.840×10^{-11}	4.149×10^{-10}	4.433×10^{-10}
Pizz2014+Lam17	2.845×10^{-11}	4.156×10^{-10}	4.441×10^{-10}
Pizz2014+Present work	2.67×10^{-11}	3.99×10^{-10}	4.26×10^{-10}
Halo Stars Observ. as in Sbordone et al. (2010)			$(1.58_{-0.28}^{+0.35}) \times 10^{-10}$

Note. The first three rows display the primordial abundances using the ${}^7\text{Be}(n, \alpha){}^4\text{He}$ reaction rates of Hou et al. (2015) (Hou2015), Lamia et al. (2017) (Lam17), and the present work. The last row refers to the ${}^7\text{Li}$ abundance for halo stars as reported in Sbordone et al. (2010).

Therefore, the integrated THM data have been corrected for the penetration factor ($l = 1$) via the standard formula

$$P_l(kr) = \frac{1}{kr(j_l^2(kr) + n_l^2(kr))}, \quad (2)$$

with j_l and n_l being the spherical Bessel and the Neumann functions, respectively. The interaction radius has been calculated via the formula $r = r_0(A_n^{1/3} + A_{7\text{Be}}^{1/3})$, with $r_0 = 1.3$ fm. In order to deduce the THM result in absolute units, a normalization to the measurements of Hou et al. (2015) was performed. In more detail, the data of Hou et al. (2015) have been first-fitted via Breit–Wigner shapes with the purpose of deducing an analytical function describing their trend. The obtained function was then spread out for the experimental energy resolution of ~ 300 keV of the present THM investigation. Thus, the normalization factor was deduced by requiring that the total area below the THM cross section data (over the whole energy range) be the same as that of the spread one (i.e., its integral) describing the data of Hou et al. (2015). This procedure led to an overall uncertainty of $\sim 15\%$, while the choice of r_0 in the penetration factor introduced an uncertainty of less than 10%. The result of the present THM investigation is shown in Figure 10 as blue filled squares with corresponding statistical uncertainties. The THM data span a broad energy region, i.e., from ~ 30 keV up to ~ 2 MeV, providing the cross section in the region of interest for big bang nucleosynthesis. The THM investigation nicely overlaps with the direct data of Kawabata et al. (2017) (red points), and at lower energies with the ones derived via CSH in Hou et al. (2015; black points). Additionally, the present results agree with the ones derived in Lamia et al. (2017; green and purple filled squares). In the same figure, the dashed line refers to the evaluation of the total s -wave component for the present reaction as derived in Barbagallo et al. (2016), while the solid line represents the ENDF/B-VII.1 evaluation by Chadwick et al. (2011). Even if the uncertainties affecting the experimental data are quite large, in some energy regions, such as those close to the 1 MeV and the 3 MeV resonances, the ENDF/B-VII.1 calculation deviates from the experimental data present in the literature while its overall trend qualitatively agrees with them.

5. Reaction Rate Calculation

The experimental data of Figure 10 (blue filled squares with their errors) have been then interpolated with the goal of having

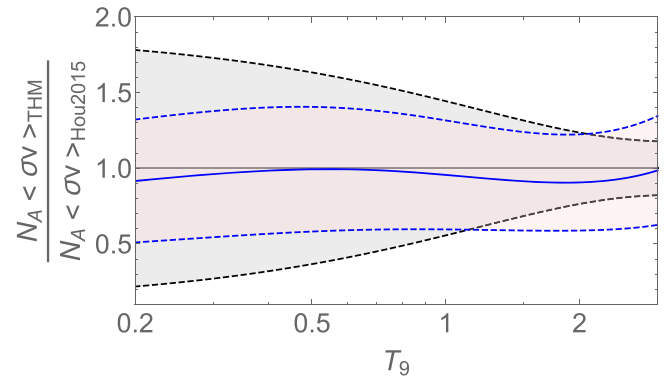


Figure 11. Ratio between the THM ${}^7\text{Be}(n, \alpha){}^4\text{He}$ reaction rate (blue solid line) and that by Hou et al. (2015) (black solid line). The red area within the blue dashed lines corresponds to the region allowed due to the experimental uncertainties on the THM data, while the gray area within the black dashed lines refers to the uncertainties in the data by Hou et al. (2015).

a smooth energy function describe the trend of the THM data. Then, the reaction rate was calculated by means of the standard formula of Rolfs & Rodney (1988);

$$N_A \langle \sigma v \rangle = \left(\frac{8}{\pi \mu} \right)^{\frac{1}{2}} \frac{N_A}{k T_9^{\frac{3}{2}}} \int_0^{\infty} E \sigma(E) e^{-\frac{E}{kT}} dE \times (\text{cm}^3 \text{mol}^{-1} \text{s}^{-1}), \quad (3)$$

where the temperature T_9 is expressed in units of 10^9 K and the center-of-mass energy E is in MeV. The THM reaction rate (together with its upper and lower values) is reported in Table 1. It has been compared with the one of Hou et al. (2015) and shows a fair agreement inside the present uncertainties that are significantly lower with respect to those of Hou et al. (2015). The result of this comparison is reported in Figure 11.

To evaluate the impact of the present reaction rate, devoted calculations have been performed via the revised BBN code of Kawano (1988) discussed in Pizzone et al. (2014). Table 2 reports three different calculations in which the primordial lithium abundances have been calculated using the already published reaction rates of Hou et al. (2015) and Lamia et al. (2017) (first two lines) and the present work (third line). The final lithium abundances (third column of Table 2) remain larger than that deduced by Sbordone et al. (2010) for halo-star observations, i.e., $(1.58_{-0.28}^{+0.35}) \times 10^{-10}$, thus once again suggesting the need of alternative solutions for the long-standing lithium problem.




6. Conclusions

The ${}^7\text{Be}(n, \alpha){}^4\text{He}$ reaction was discussed here in the framework of the primordial big bang nucleosynthesis because of its role in the cosmological lithium problem. The ${}^7\text{Be}$ -n reaction was investigated by means of the THM applied to the quasi-free ${}^2\text{H}({}^7\text{Be}, \alpha){}^4\text{He}$ p reaction, once the reaction channel and reaction mechanism were selected properly. The binary cross section extracted here allowed us, for the first time, to span a wide range in energy in a single experiment overlapping both the high-energy region and the one of interest for BBN. In addition to the abovementioned agreement, also note that the present THM investigation significantly reduces the uncertainty in the BBN energy region, thus further constraining the nuclear physics input for the cosmological lithium problem.

To complete the present picture of THM investigations of ${}^7\text{Be}$ neutron-induced reactions, further efforts are necessary. These are already ongoing with the aim of investigating the (n, α) and (n, p) channels right in the region of interest for SBBN. In conclusion, the present study represents the first THM measurement in which a reaction involving both a radioactive beam and neutrons is studied. This represents a crucial step for THM application because the present validation could open new frontiers for studying neutron-induced reactions with short-lived RIB's of relevance for astrophysics.

This work has been partially supported by the Italian Ministry of the University under grant RBF082838 and "LNS-Astrofisica Nucleare (fondi premiali)." J.M. and G.D'A. acknowledge MEYS, under the project SPIRAL2-CZ, EF16-013/0001679. C. A.B. acknowledges support from the U.S. NSF grant No 1415656 and the U.S. DOE grant No. DE-FG02-08ER41533. S.H. acknowledges "JSPS KAKENHI (grant No. 15K17631)."

ORCID iDs

L. Lamia  <https://orcid.org/0000-0002-4055-0811>
 C. A. Bertulani  <https://orcid.org/0000-0002-4065-6237>
 G. D'Agata  <https://orcid.org/0000-0001-5261-8329>

References

- Ade, P. A. R., Aghanim, N., Arnaud, M., et al. Planck Collaboration XIII 2016, *A&A*, **594**, A13
- Assenbaum, H., Langanke, K. L., & Rolfs, C. 1987, *ZPhyA*, **327**, 461
- Barbagallo, M., Musumarra, A., Cosentino, L., et al. 2016, *PhRvL*, **117**, 152701
- Baur, G. 1986, *PhLB*, **178**, 135
- Bemmerer, D., Confortola, F., Costantini, H., et al. 2006, *PhRvL*, **97**, 122502
- Bertulani, C. A., & Kajino, T. 2016, *PhPNP*, **89**, 56
- Broggini, C., Canton, L., Fiorentini, G., & Villante, F. L. 2012, *JCAP*, **6**, 030
- Cassagnou, Y., Jeronimo, J. M. F., Mani, G. S., Sadeghi, A., & Forsyth, P. D. 1962, *NuPhA*, **33**, 449
- Chadwick, M. B., Herman, M., Obložinský, P., et al. 2011, *NDS*, **112**, 2887
- Cherubini, S., Gulino, M., Spitaleri, C., et al. 2015, *PhRvC*, **92**, 015805
- Coc, A., Uzan, J.-P., & Vangioni, E. 2013, *PhRvD*, **87**, 123530
- Cooke, R. J. 2015, *ApJL*, **812**, L12
- Cybur, R. H., Ellis, J., Fields, B. D., et al. 2013, *JCAP*, **5**, 014
- di Leva, A., Gialanella, L., Kunz, R., et al. 2009, *PhRvL*, **102**, 232502
- Farinon, F., Glodariu, T., Mazzocco, M., et al. 2008, *NIMPB*, **266**, 4097
- Fu, X., Bressan, A., Molaro, P., & Marigo, P. 2015, *MNRAS*, **452**, 3256
- Goudelis, A., Pospelov, M., & Pradler, J. 2016, *PhRvL*, **116**, 211303
- Guardo, G. L., Spitaleri, C., Lamia, L., et al. 2017, *PhRvC*, **95**, 025807
- Hammache, F., Coc, A., de Séréville, N., et al. 2013, *PhRvC*, **88**, 062802
- Hartos, M., Bertulani, C. A., Shubhchintak, Mukhamedzhanov, A. M., & Hou, S. 2018, *ApJ*, **862**, 62
- Hou, S. Q., He, J. J., Kubono, S., & Chen, Y. S. 2015, *PhRvC*, **91**, 055802
- Hou, S. Q., He, J. J., Parikh, A., et al. 2017, *ApJ*, **834**, 165
- Indelicato, I., La Cognata, M., Spitaleri, C., et al. 2017, *ApJ*, **845**, 19
- Izotov, Y. I., Thuan, T. X., & Guseva, N. G. 2014, *MNRAS*, **445**, 778
- Kawabata, T., Fujikawa, Y., Furuno, T., et al. 2017, *PhRvL*, **118**, 052701
- Kawano, L. 1988, FERMLAB Rep. No. PUB-88/34-A, unpublished
- Kelley, J., et al. 2012, *NuPhA*, **880**, 8
- King, C. H., Austin, S. M., Rossner, H. H., & Chien, W. S. 1977, *PhRvC*, **16**, 1712
- La Cognata, M., Mukhamedzhanov, A. M., Spitaleri, C., et al. 2011, *ApJL*, **739**, L54
- La Cognata, M., Spitaleri, C., Trippella, O., et al. 2013, *ApJ*, **777**, 143
- Lamia, L., La Cognata, M., Spitaleri, C., Irgaziev, B., & Pizzone, R. G. 2012, *PhRvC*, **85**, 025805
- Lamia, L., Spitaleri, C., Bertulani, C. A., et al. 2017, *ApJ*, **850**, 175
- Lamia, L., Spitaleri, C., Tognelli, E., et al. 2015, *ApJ*, **811**, 99
- LEP Collaborations 2006, *PhR*, **427**, 257
- Mazzocco, M., Torresi, D., Strano, E., et al. 2013, *NIMPB*, **317**, 223
- Mukhamedzhanov, A. M., Blokhintsev, L. D., Irgaziev, B. F., et al. 2008, *JPhG*, **35**, 014016
- Nordlander, T., Korn, A. J., Richard, O., & Lind, K. 2012, *ApJ*, **753**, 48
- Patrignani, C. & Particle Data Group 2016, *ChPhC*, **40**, 100001
- Pettini, M., & Cooke, R. 2012, *MNRAS*, **425**, 2477
- Pierroutsakou, D., Boiano, A., Boiano, C., et al. 2016, *NIMPA*, **834**, 46
- Pitrou, C., Coc, A., Uzan, J.-P., & Vangioni, E. 2018, *PhR*, **754**, 1
- Pizzone, R. G., Roeder, B. T., McCleskey, M., et al. 2016, *EPJA*, **52**, 24
- Pizzone, R. G., Spartá, R., Bertulani, C. A., et al. 2014, *ApJ*, **786**, 112
- Pizzone, R. G., Spitaleri, C., Cherubini, S., et al. 2005, *PhRvC*, **71**, 058801
- Pizzone, R. G., Spitaleri, C., Mukhamedzhanov, A. M., et al. 2009, *PhRvC*, **80**, 025807
- Rijal, N., Wiedenhöver, I., Blackmon, J. C., et al. 2018, arXiv:1808.07893
- Rolfs, C., & Rodney, W. 1988, *Cauldrons in the Cosmos* (Chicago, IL: Univ. Chicago Press)
- Sbordone, L., Bonifacio, P., Caffau, E., et al. 2010, *A&A*, **522**, A26
- Sergi, M. L., Spitaleri, C., La Cognata, M., et al. 2015, *PhRvC*, **91**, 065803
- Slobodrian, R. J., et al. 1975, *ZPhyA*, **342**, 471
- Spitaleri, C. 1991, in *Problems of Fundamental Modern Physics, II: Proc. 21 Spitaleri, C., La Cognata, M., Lamia, L., Mukhamedzhanov, A. M., & Pizzone, R. G. 2016, EPJA, 52, 77*
- Spitaleri, C., Lamia, L., Tumino, A., et al. 2004, *PhRvC*, **69**, 055806
- Steigman, G. 2006, in *Proc. Space Telescope Science Institute Symp. 17*, 16
- Tribble, R. E., Bertulani, C. A., La Cognata, M., Mukhamedzhanov, A. M., & Spitaleri, C. 2014, *RPPh*, **77**, 106901
- Tumino, A., Spitaleri, C., La Cognata, M., et al. 2018, *Natur*, **557**, 687
- Weiland, J. L., Odegard, N., Hill, R. S., et al. 2011, *ApJS*, **192**, 19
- Zadro, M., Miljanić, D., Spitaleri, C., et al. 1989, *PhRvC*, **40**, 181